ELSEVIER

Contents lists available at ScienceDirect

Chemical Engineering Journal

journal homepage: www.elsevier.com/locate/cej



Mechanistic study of Hg^0 oxidation over LaMnO₃ oxygen carrier during chemical looping combustion

Zhongze Bai a, Kai H. Luo a,b,*

ARTICLE INFO

Keywords: Mercury oxidation LaMnO₃ Density functional theory Chemical looping combustion Reaction mechanisms

ABSTRACT

LaMnO₃, known for its high thermal stability, redox activity and cost-effectiveness, is a promising material for coal chemical looping combustion (CLC). Density functional theory (DFT) calculations are carried out to investigate the catalytic mechanisms of Hg^0 oxidation by oxygen species (lattice oxygen, perpendicularly adsorbed O_2 and dissociative adsorbed O_2) on the LaMnO₃(010) surface. The results indicate that Hg^0 , HgO and HgO and HgO and HgO and HgO oxidation proceeds via a consistent three-step mechanism: $Hg^0 \to Hg$ (ads) HgO oxidation proceeds via a consistent three-step mechanism: $Hg^0 \to Hg$ (ads) HgO oxidation featuring the lowest rate-limiting energy barrier (1.354 eV), thus representing the most favourable pathway. This study elucidates the adsorption and oxidation mechanisms of Hg^0 on the LaMnO₃(010) surface, offering microscopic insights into its catalytic role in mercury removal. These findings would provide a theoretical foundation for developing efficient and low-emission Hg^0 control strategies.

1. Introduction

Direct combustion of coal produces huge amounts of CO_2 , which acts as a major source of global warming [1–3]. To address this problem, researchers have explored a wide range of technologies aimed at mitigating its impact, with chemical looping combustion (CLC) emerging as a particularly promising solution [4,5]. In a CLC system, oxygen carriers (OCs) transfer oxygen from the air reactor to the fuel reactor, effectively eliminating direct contact between air and fuel [6,7]. This unique process allows for the efficient separation of pure CO_2 by condensing $\mathrm{H}_2\mathrm{O}$ from the exhaust stream of the fuel reactor. Therefore, CLC is widely recognized as a cost-effective and highly efficient carbon capture technology.

In the CLC system, OCs play a pivotal role in determining overall efficiency and performance [8,9]. Various materials have been explored as OCs in CLC, including single metal oxides, single non-metallic oxides, composite oxides, perovskite oxides, etc. [10]. Among these, perovskite oxides have attracted considerable interests due to their high reactivity, outstanding thermal stability, and cost-effectiveness [11,12]. Perovskite materials are commonly represented by the formula ABO₃ [13]. In this structure, the A-site, enclosed by 12 oxygen atoms, is typically occupied

by rare earth or alkaline earth metals with relatively large atomic radii, while the B-site, coordinated with 6 oxygen atoms, is usually occupied by transition metals with smaller cationic radii [14].

LaMnO₃, a representative Mn-based perovskite oxide, is well known for its high thermal stability, superior redox activity and low cost, making it a prominent material for CLC applications [15,16]. Notably, Ma et al. conducted experimental and theoretical studies to explore the reactivity and microscopic reaction mechanisms of LaMnO₃ with CO in CLC [15]. Sarshar and co-workers prepared LaMnO3 using the nanocasting method, demonstrating its high α -O₂ availability and excellent reducibility for CH₄-based CLC [17]. LaMnO₃ exhibited stable performance, effectively preventing CO formation under low CH₄ pressure [17]. Additionally, they developed LaMn_{0.7}Fe_{0.3}O_{3.15}@mSiO₂ coreshell structures, which demonstrated both high reactivity and stability for CH₄ combustion [18]. Iliopoulou et al. synthesized La_{1-x}Ca_xMnO₃ OCs via the coprecipitation method and demonstrated their excellent stability over eight successive redox cycles at 1000 °C during CH₄-based CLC [19]. However, previous studies have primarily focused on the reactivity of LaMnO3-based oxygen carriers in the CLC process, while neglecting the influence of potential pollutants generated during coal CLC. These pollutants can lead to equipment corrosion, oxygen carrier

^a Department of Mechanical Engineering, University College London, Torrington Place, London WC1E 7JE, UK

b Center for Combustion Energy, Department of Energy and Power Engineering, Key Laboratory for Thermal Science and Power Engineering of Ministry of Education, Low Carbon Energy and CCUS Research Center, Institute for Carbon Neutrality, Tsinghua University, 10084 Beijing, China

^{*} Corresponding author at: Department of Mechanical Engineering, University College London, Torrington Place, London WC1E 7JE, UK. E-mail address: k.luo@ucl.ac.uk (K.H. Luo).

degradation, environmental concerns and a reduction in the purity of captured CO_2 [20,21].

According to recent reports from the World Health Organization (WHO) and the United Nations Environment Programme (UNEP), coal combustion remains the largest anthropogenic source of atmospheric mercury emissions, accounting for approximately 21 % of global releases (approximately 2220 t annually) [22,23]. Mercury (Hg) is a typical trace element in coal, inevitably released during coal combustion and converted into elemental mercury (Hg⁰), oxidized mercury (Hg²⁺) and particulate mercury (HgP) [24,25]. Among these species, Hg0 dominates emissions due to its chemical inertness and low water solubility, presenting a significant challenge for effective mitigation [24,25]. In chemical looping combustion (CLC) systems, the interaction between mercury species and oxygen carriers plays a pivotal role in determining pollutant removal efficiency. Wang and co-workers utilized density functional theory (DFT) calculations to elucidate the fundamental mechanisms of Hg⁰ oxidation by HCl on the LaMnO₃ surface [26]. However, their study did not consider the direct oxidation of Hg⁰ by LaMnO₃ itself, which is a crucial pathway in coal CLC, particularly for coals with low Cl content [27].

To address this gap, we employed DFT calculations, a powerful computational approach for elucidating electronic structures and reaction pathways at the atomic level [20], to investigate the reaction mechanisms of ${\rm Hg}^0$ on the LaMnO $_3$ surface. Firstly, the adsorption behaviours of ${\rm Hg}^0$, ${\rm O}_2$ and ${\rm HgO}$ on the LaMnO $_3$ surface were examined. In addition, the transition states and energy profiles of potential ${\rm Hg}^0$ oxidation pathways were analysed to gain deeper insight into the underlying oxidation mechanisms.

2. Methods

2.1. Computational details

All DFT calculations were performed using the Vienna Ab Initio Simulation Package (VASP) [28,29], within the framework of the generalized gradient approximation (GGA) and employing the Perdew-Burke-Ernzerhof (PBE) functional [30]. A plane wave energy cutoff of 500 eV was applied, with convergence criteria for the total energy and forces set to 1.0×10^{-5} eV and 0.03 eV/Å, respectively. Monkhorst-Pack k-point grids of $5 \times 4 \times 5$ and $2 \times 2 \times 1$ were employed for the unit cell and supercell of LaMnO₃, respectively. The computational parameters were primarily derived from the existing literature [15,16,26]; however, the energy cutoff value has been increased to 500 eV to enhance the accuracy and reliability of the calculations. The climbing image nudged elastic band (CI-NEB) method was utilized to locate the transition state (TS) and determine the reaction barriers [31]. The CI-NEB calculations employed the same computational settings as those used in the static calculations, including the exchange-correlation functional, energy cutoff, k-point sampling, and convergence criteria. The validity of the obtained TS structures was confirmed by vibrational frequency analysis. The calculations were facilitated using the VASPKIT [32] and QVASP [33] software packages. The visualizations were generated using the VESTA software [34].

The adsorption energy (E_{ads}), energy barrier (E_b) and overall reaction energy (E_{all}) are determined using Eqs. (1)–(3), respectively.

$$E_{\text{ads}} = E(AB) - E(A) - E(B) \tag{1}$$

$$E_{\rm b} = E({\rm TS}) - E({\rm IS}) \tag{2}$$

$$E_{\text{all}} = E(FS) - E(IS) \tag{3}$$

where *E*(AB), *E*(A), *E*(B), *E*(TS), *E*(IS) and *E*(FS) are the energies of adsorption structure, substrate, adsorbate, transition state, initial state and final state, respectively. Zero-point energy (ZPE) corrections were applied to adsorption and activation energies based on vibrational

frequency calculations.

2.2. Computational models

The unit cell of LaMnO3 is an orthorhombic structure with a Pnma space group from the Materials Project database (MP-17554) [35]. The optimized LaMnO₃ unite cell is presented in Fig. 1a. The LaMnO₃(010) surface demonstrates both energetic stability and catalytic activity [36]. Previous simulations show that Hg⁰ adsorption on the La-terminated surface is primarily physisorption and weaker than the chemisorption on the Mn-terminated (010) surface [26]. Thermodynamic studies indicate that below 927 °C, the Mn-terminated LaMnO₃ surface is more stable than the La-terminated one, suggesting that Mn-terminated surfaces dominate under practical conditions [37]. Experimentally, Hg⁰ capture efficiency by LaMnO $_3$ increases with temperature from 100 $^{\circ}\text{C}$ to 150 °C, consistent with a chemisorption mechanism [38-40]. Based on these findings, the Mn-terminated LaMnO₃ (010) surface was selected for modelling in this study. A p(2 \times 2) supercell consisting of eight atomic layers was constructed with a 20 Å vacuum layer incorporated to eliminate interactions between periodic slabs. To improve computational efficiency, during structural optimization, the top four layers were allowed to relax, while the bottom four layers were kept fixed. After geometric optimization, the LaMnO₃(010) surface (Fig. 1b) revealed six potential active sites: Mn, O₁, O₂, bridge₁, bridge₂ and hollow. All surface models employed in our calculations were fully relaxed prior to adsorption and transition state simulations.

3. Results and discussion

3.1. Interaction of Hg⁰ and HgO on LaMnO₃ surface

As the reactant and final product, respectively, understanding the adsorption behaviours of Hg⁰ and HgO on the LaMnO₃(010) surface are the fundamental prerequisite for elucidating the catalytic oxidation mechanism of Hg⁰. After evaluating six possible adsorption sites on the LaMnO₃(010) surface (Fig. 1b), four stable configurations are identified, as shown in Fig. 2. The corresponding adsorption energies and Bader charges are provided in Table 1. The adsorption strength of the four configurations decreases in the following order: 1B > 1D > 1A > 1C. The most stable structure for Hg⁰ adsorption is 1B, where Hg⁰ adsorbs onto Mn, forming a Hg-Mn bond, which is consistent with previous work [26]. The binding energy of 1B is -0.226 eV with a Bader charge transfer of -0.04 e, indicating chemical adsorption of Hg^0 . In configurations 1A, 1C, and 1D, Hg⁰ is adsorbed at the hollow, O₁, and O₂ sites, respectively, with relatively low binding energies of -0.043 eV, -0.033eV and -0.156 eV. The corresponding Bader charge transfers are negligible, suggesting that Hg⁰ adsorption in these cases is dominated by physisorption.

It is worth noting that the binding energy and charge transfer values for the 1B configuration exhibit slight deviations from those reported in previous studies [26], due to differences in the computational software,

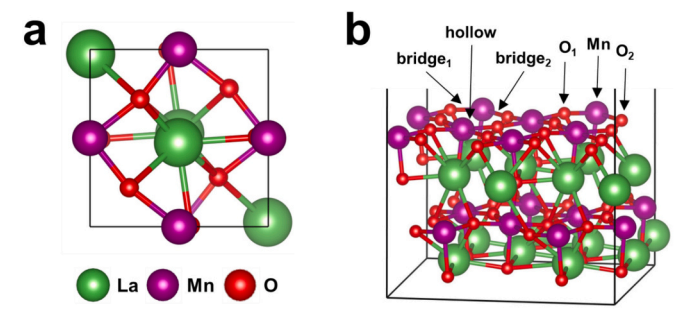


Fig. 1. Schematic representation of the LaMnO $_3$ (010) surface. (a) unit cell of LaMnO $_3$; (b) Mn-terminated LaMnO $_3$ (010) surface.

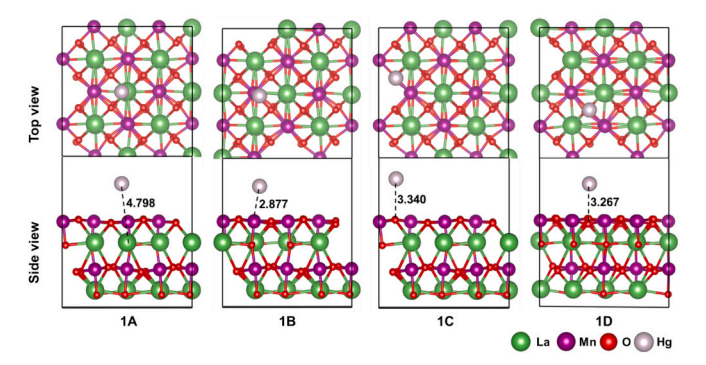


Fig. 2. Adsorption configurations of ${\rm Hg}^0$ on LaMnO₃(010) surface. The unit for bond length is Å.

Table 1 Summary of adsorption energies ($E_{\rm ads}$, eV) and Bader charge transfer (Q, e) for Hg⁰ adsorption on LaMnO₃(010) surface (1A-1C), HgO adsorption on LaMnO₃(010) surface (2A-2H), O₂ adsorption on LaMnO₃(010) surface (3A-3C) and Hg⁰ adsorption on oxygen covered LaMnO₃(010) surface (4A-4H). A negative charge transfer value indicates electron transfer from the adsorbate to the surface.

ID	$E_{ m ads}$	Q	ID	$E_{\rm ads}$	Q
1A	-0.043	0.00	3A	-4.909	0.94
1B	-0.226	-0.04	3B	-4.975	1.04
1C	-0.033	0.00	3C	-2.578	0.43
1D	-0.156	-0.01	4A	-0.242	-0.12
2A	-1.756	0.27	4B	-0.209	-0.10
2B	-1.356	0.03	4C	-0.268	-0.13
2C	-1.345	0.03	4D	-0.222	-0.10
2D	-4.563	0.44	4E	-0.072	-0.04
2E	-4.562	0.45	4F	-0.275	-0.12
2F	-4.622	0.43	4G	-0.187	-0.10
2G	-4.674	0.44	4H	-0.063	-0.02
2H	-4.446	0.52			

parameters and charge analysis methods used. Specifically, CASTEP and VASP employ distinct DFT algorithms, which can influence both the energy and charge distributions. Additionally, Mulliken and Bader charge analyses use different approaches for partitioning the electron density, resulting in variations in the charge values. Considering that the overall conclusions regarding ${\rm Hg}^0$ adsorption remain consistent, these variations can be regarded as a normal outcome inherent to the computational methodologies employed.

For HgO adsorption on the LaMnO₃(010) surface, six possible adsorption sites and orientations, both perpendicular (Hg-down and Odown) and parallel, are systematically explored. Eight stable structures (2A-2H) are identified, as illustrated in Fig. 3. The corresponding adsorption energies and Bader charge transfers are summarized in Table 1. There are three stable configurations for the perpendicular (Hgdown) orientation of HgO adsorption, wherein the Hg atom adsorbs onto the Mn (2A), O1 (2B), and O2 (2C) sites, respectively. The binging configuration of 2A is the most stable with adsorption energy and Bader charge transfer of -1.756 eV and 0.27 e, respectively. For the perpendicular (O-down) orientation of HgO adsorption (2H), the O atom binds to a Mn site forming an O-Mn bond; however, the Hg-O bond is broken, with a bond length of 3.092 Å, indicating that a stable HgO adsorption structure cannot be formed. In the parallel orientation of HgO adsorption, the Hg and O atoms form bonds with Mn atoms on the LaMnO₃(010) surface, resulting in the formation of Hg-Mn and O-Mn bonds. Depending on the relative positions of the two Mn atoms involved in bonding, four different adsorption configurations (2D-2G) are obtained. In all parallel adsorption cases, the Hg—O bond is broken, indicating dissociative adsorption of HgO. Notably, for configurations involving molecular dissociation upon adsorption (such as 2D-2H, 3A,

and 3B), the calculated adsorption energy reflects not only the molecule–surface interaction but also the energy gain from bond cleavage. Therefore, it no longer directly represents the stability of the intact HgO molecule on the surface. In such cases, the adsorption energy reported in Table 1 are the total stabilization energy of the dissociated configuration, rather than the binding energy of the intact molecule.

To gain deeper insight into the adsorption mechanisms of Hg^0 and HgO on the LaMnO₃(010) surface, projected density of states (PDOS) analysis is performed for their most stable adsorption configurations (1B and 2A). Fig. 4a and b presents the projected density of states (PDOS) for Hg and Mn atoms in configurations 1B and 2A, respectively. Overall, the Hg 5d orbital is fully occupied and lies at relatively low energies (around -6 eV) under both Hg and HgO adsorption conditions, making it chemically inert and contributing little to the Hg-Mn bonding interactions. In the Hg adsorption configuration, the Hg-s orbital exhibits hybridization with the Mn-d orbital around -2.5 eV. In contrast, under the HgO adsorption configuration, the Hg-s orbital shows stronger hybridization with the Mn-d orbital at a similar energy level (around -2.5eV), and additionally, the Hg-p orbital displays hybridization with the Mn-d orbital around -0.9 eV. These features indicate a stronger Hg—Mn interaction in the HgO case, which corresponds to a more robust adsorption strength in the 2A configuration. That is consistent with the result that the adsorption energy of HgO is more negative than that of Hg⁰ on LaMnO₃(010) surface.

3.2. O2 adsorption on the LaMnO3 surface

Under high-temperature conditions in chemical looping combustion, LaMnO₃(010) can release lattice oxygen to form O₂ which may adsorb on the surface and significantly affect the oxidation mechanisms of Hg^0 and the catalytic performance. Therefore, a systematic investigation of O₂ adsorption configurations and surface sites is essential to better understand the catalytic activity and heterogeneous oxidation pathway of Hg^0 . All possible adsorption orientations (perpendicular and parallel) and adsorption sites are considered during calculations. The optimized configurations of O₂ adsorption on the LaMnO₃(010) surface are presented in Fig. 5, while the corresponding adsorption energies and Bader charge transfers are summarized in Table 1.

There are three stable configurations for O2 adsorption on the $LaMnO_3(010)$ surface, including two parallel adsorption structures (3A and 3B) and one perpendicular adsorption structure (3C). In the 3A and 3B configurations, each oxygen atom forms a bond with an adjacent Mn atom, resulting in the dissociation of the O—O bond. Under the parallel adsorption mode of O2, each oxygen atom forms a bond with a neighboring Mn atom, resulting in the dissociation of the O-O bond. Depending on the identity of the surface oxygen atom (O₁ and O₂ sites in Fig. 1) located between the two adjacent Mn atoms involved in bonding, two distinct configurations (3A and 3B in Fig. 5) are identified. These configurations are denoted as A-C-B types, where atom C lies between the two adsorption sites A and B. Accordingly, the two configurations are herein referred to as the Mn-O1-Mn and Mn-O2-Mn adsorption structures, respectively. The adsorption energies for these configurations are -4.909 eV and -4.975 eV, respectively, with corresponding charge transfers of 0.94 e and 1.04 e. The O-O bond lengths for 3A and 3B configurations are 3.882 Å and 3.661 Å, respectively. In the perpendicular adsorption configuration of O2 (3C), one oxygen atom binds to a surface Mn atom, forming an O—Mn bond with an adsorption energy of -2.578 eV and a Bader charge transfer of 0.43 e. Given the significant charge transfer and strong interaction with the surface, the adsorption of O₂ in this configuration is characteristic of chemisorption. The O2 molecule remains intact without dissociation and is stably adsorbed on the LaMnO₃(010) surface. The O-Mn and O-O bond lengths are 1.739 Å and 1.292 Å, respectively.

Previous studies have demonstrated that O_2 molecule dissociation is a key step that significantly influences the overall oxidation process [41]. Consequently, we subsequently investigated the dissociation

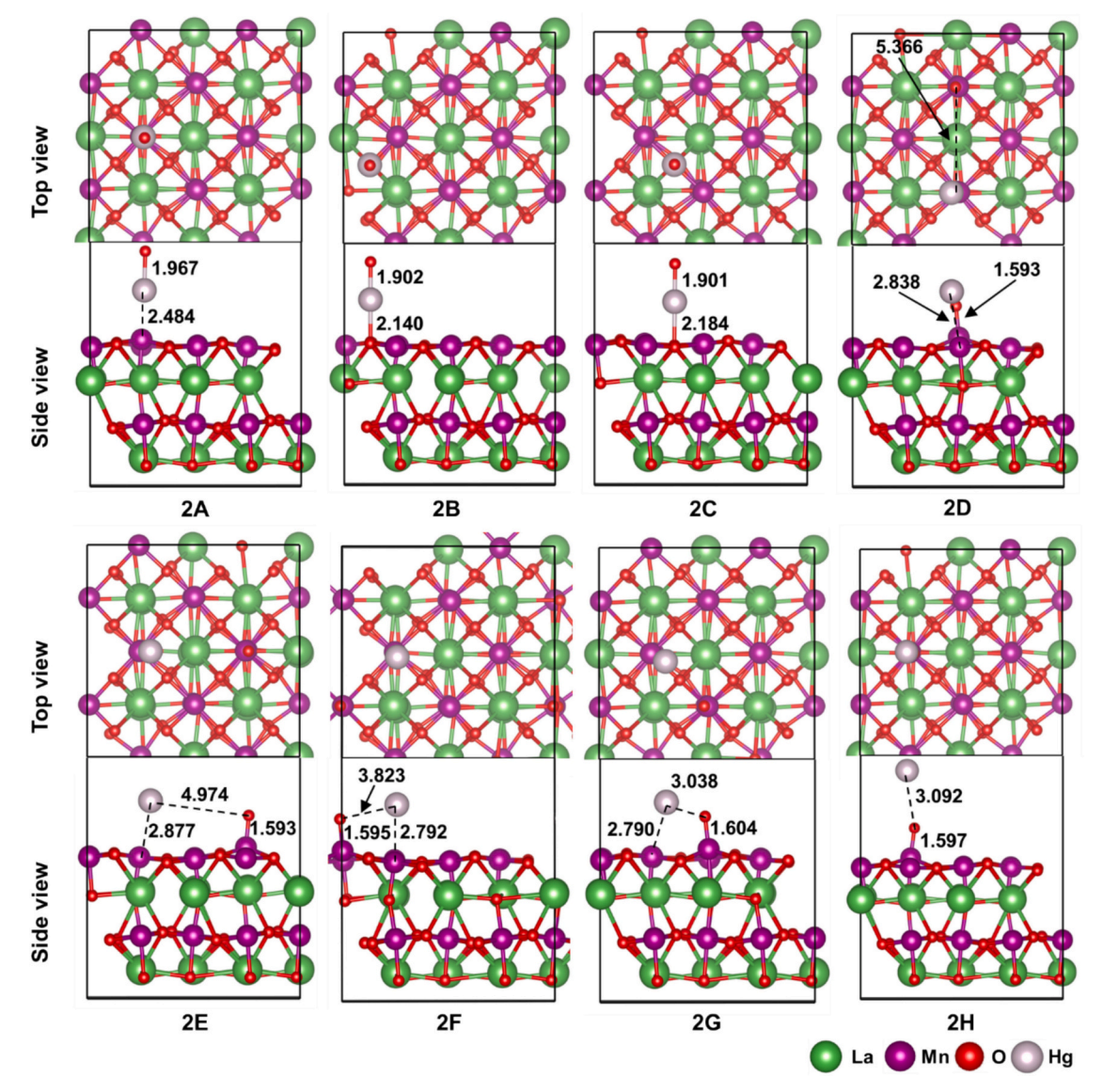


Fig. 3. Adsorption configurations of HgO on LaMnO₃(010) surface. The unit for bond length is Å.

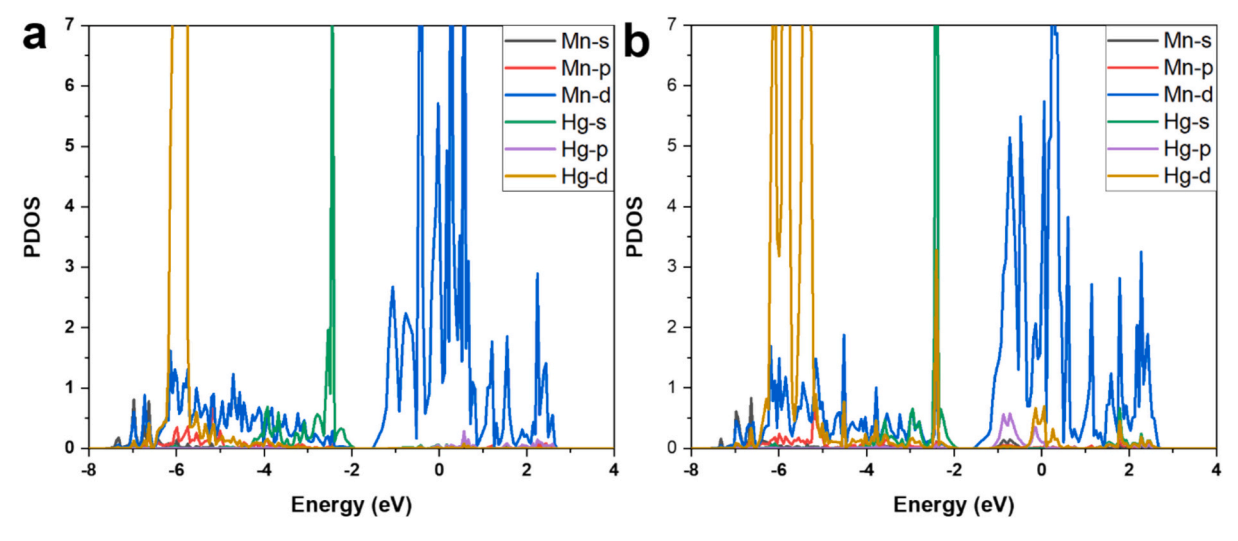


Fig. 4. PDOS of Hg and Mn atoms for configurations (a) 1B and (b) 2A.

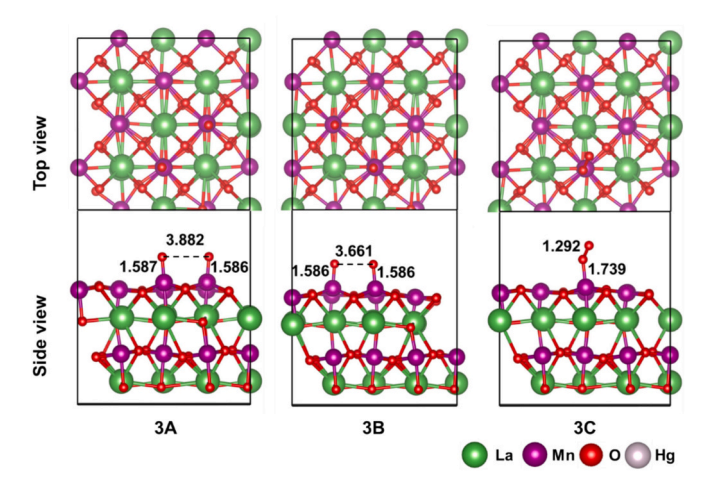


Fig. 5. Adsorption configurations of ${\rm O_2}$ on LaMnO₃(010) surface. The unit for bond length is Å.

behaviour of O_2 on the LaMn O_3 surface. Fig. 6 illustrates the energy profile along with the optimized geometries of the intermediate (IM), transition state (TS) and final state (FS). O_2 adsorption serves as the initial step, forming the intermediate IM1 (3C in Fig. 5). From IM1, two possible dissociation pathways of O_2 are identified. In the first pathway (IM1 \rightarrow TS1 \rightarrow FS1, corresponding to 3A in Fig. 5), the dissociation process is exothermic, releasing 2.331 eV of energy, with an activation energy barrier of 1.470 eV. During this process, the O—O bond progressively elongates and eventually dissociates, with bond lengths increasing from 1.292 Å in IM1 to 1.355 Å in TS1, and reaching 3.882 Å in FS1. In the second pathway (IM1 \rightarrow TS2 \rightarrow FS2, corresponding to 3B in Fig. 5), the process is also exothermic, with an energy release of 2.397 eV and a lower energy barrier of 0.966 eV. Similarly, the O—O bond elongates and breaks during the reaction, with bond lengths of 1.292 Å in IM1, 1.384 Å in TS2, and 3.661 Å in FS2.

3.3. Hg^0 and O_2 adsorption on LaMn O_3 surface

Based on the preceding analysis, O_2 exhibits a stronger adsorption affinity on the LaMnO₃(010) surface compared to Hg⁰, suggesting that O_2 is likely to preferentially occupy surface sites and thereby influence the subsequent adsorption and oxidation behaviour of Hg⁰. Accordingly,

this section focuses on the investigation of ${\rm Hg^0}$ adsorption on ${\rm O_2}$ -covered LaMnO₃(010) surfaces. Three representative ${\rm O_2}$ adsorption configurations (3A, 3B and 3C) are considered in the computational analysis. After thoroughly exploring all potential adsorption sites, eight stable configurations are identified, as illustrated in Fig. 7. The corresponding adsorption energies and Bader charge transfers are summarized in Table 1.

In the case of perpendicular O_2 adsorption, the Hg atom preferentially binds to the neighbouring Mn atom adjacent to the adsorbed O_2 molecule. Two stable configurations (4A and 4B in Fig. 7) are identified. The Hg—Mn bond lengths are 2.765 Å and 2.792 Å, respectively. The corresponding adsorption energies are -0.242 eV and -0.209 eV, accompanied by charge transfers of 0.12 e and 0.10 e from Hg to the LaMnO₃(010) surface.

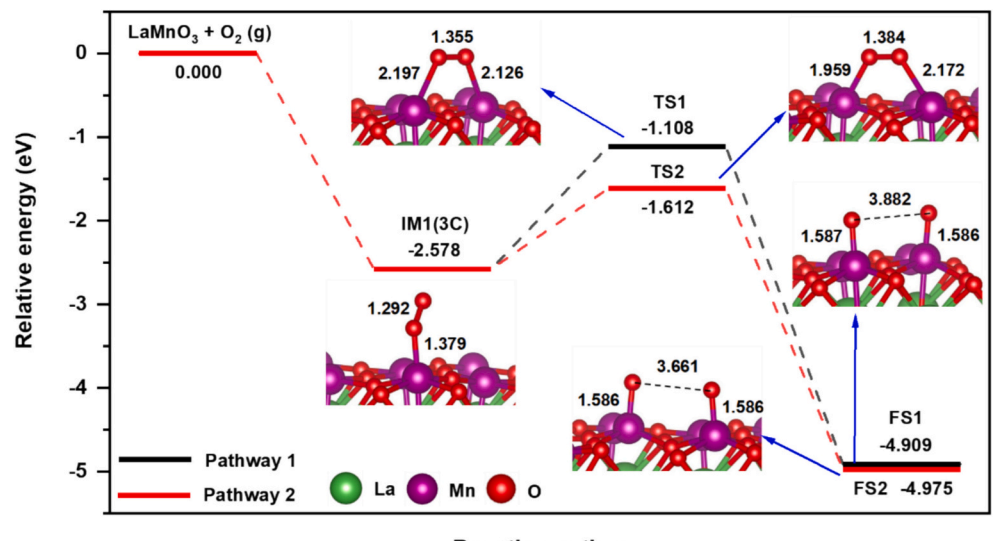
In the case of O_2 adsorption structure of 3A, two different Hg^0 adsorption types are identified. In the first type, the Hg^0 atom adsorbs onto a Mn atom adjacent to the surface oxygen, and there are two stable configurations: Mn-O₂-Mn (4C) and Mn-O₁-Mn (4D). These configurations exhibit adsorption energies of -0.268 eV and -0.222 eV, with corresponding Bader charge transfers of 0.13~e and 0.10~e, respectively. In the second type, the Hg^0 atom is adsorbed above the two oxygen atoms, forming an HgO-like bond, as represented by configuration 4E in Fig. 7. Compared to 4C and 4D, 4E shows a weaker interaction with the surface, characterized by a lower adsorption energy of -0.072 eV and a smaller charge transfer of 0.04~e.

In the situation of O_2 adsorption structure of 3B, the behaviour is similar to that of the Mn-O₁-Mn structure, with three stable Hg^0 adsorption configurations identified: 4F, 4G and 4H. The corresponding adsorption energies are -0.275 eV, -0.187 eV, and -0.063 eV, respectively, accompanied by Bader charge transfers of -0.12 e, -0.10 e and -0.02 e (Table 1).

Overall, compared with the clean surface, the presence of surface oxygen atoms has a limited impact on the adsorption energy of Hg^0 , which is consistent with previous studies [27,42]. Furthermore, the MnO₂-Mn adsorption configuration exhibits lower adsorption energy than the Mn-O₁-Mn configuration.

3.4. Reaction mechanism of Hg^0 oxidation by oxygen species on $LaMnO_3$ surface

In this section, the oxidation process of Hg^0 on the $\mathrm{LaMnO_3}(010)$ surface is systematically investigated. Based on the preceding analysis, four types of oxygen species are considered: lattice oxygen,



Reaction pathway

Fig. 6. Energy profiles and optimized structures of O2 adsorption and dissociation on LaMnO3(010) surface. The unit for bond length is Å.

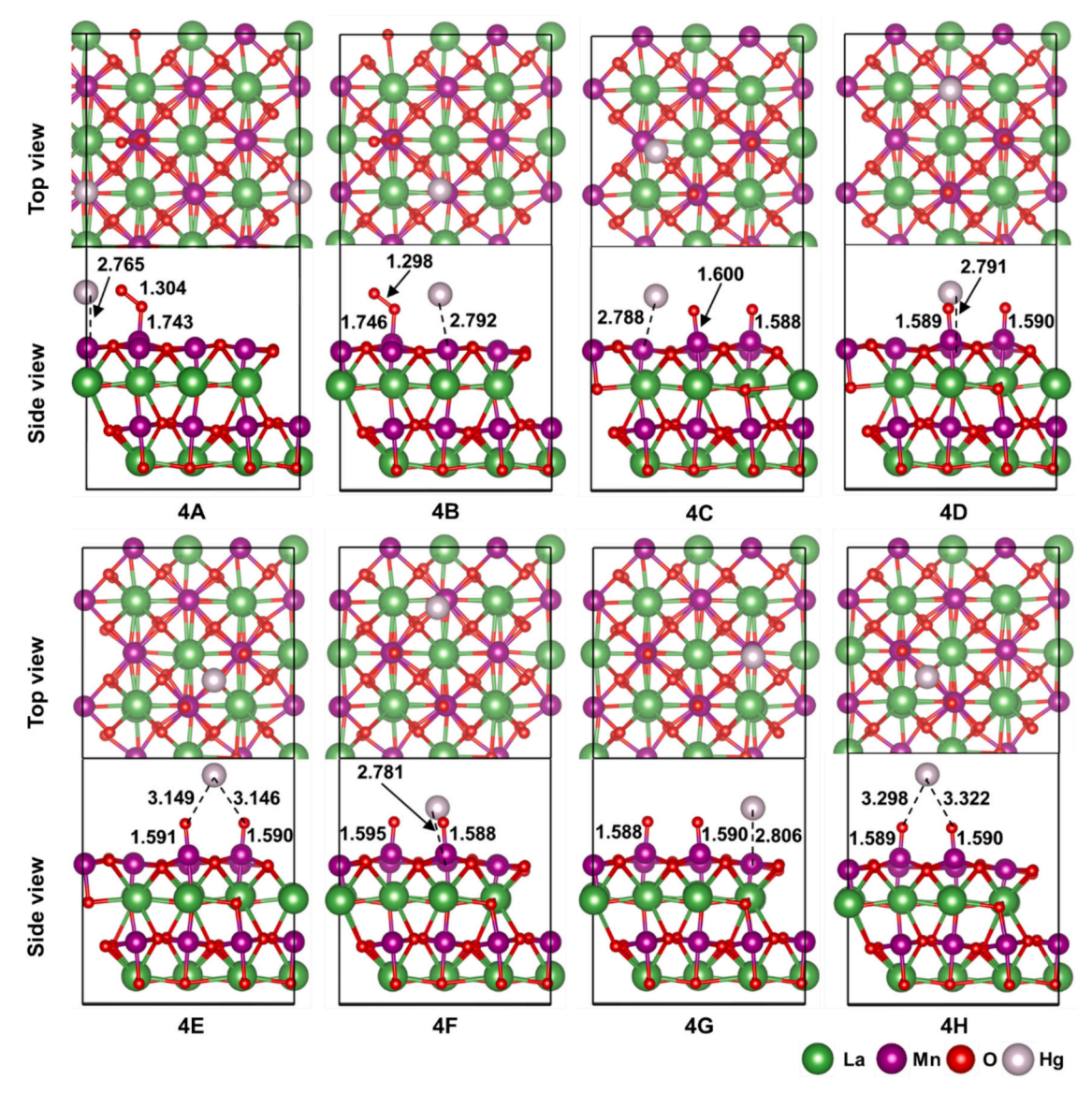


Fig. 7. Adsorption configurations of Hg⁰ on O₂-covered LaMnO₃(010) surface. The unit for bond length is Å.

perpendicularly adsorbed O_2 , dissociative adsorbed O_2 in Mn-O₁-Mn configuration and dissociative adsorbed O_2 in Mn-O₂-Mn configuration. The corresponding energy profiles for Hg^0 oxidation, along with the optimized structures of intermediates, transition states and final states, are presented in Figs. 8, 9, 10, and 11, respectively.

In the oxidation of Hg⁰ by lattice oxygen (Fig. 8), there are two different reaction pathways. In the first pathway, surface lattice oxygen O_1 oxidizes Hg^0 to $\mathrm{Hg}\mathrm{O}$, while in the second pathway, surface lattice oxygen O2 serves as the oxidizing species. Both pathways proceed through three elementary steps: $Hg^0 \rightarrow Hg$ (ads) $\rightarrow HgO$ (ads) $\rightarrow HgO$. In the first step (Hg⁰ \rightarrow Hg (ads)), a mercury atom adsorbs onto a surface Mn atom, forming the intermediate IM2 with an exothermicity of -0.226 eV. In the second step (Hg (ads) \rightarrow HgO (ads)), two unique pathways are identified. In Pathway 1, the adsorbed Hg⁰ atom migrates from the Mn site to the surface oxygen site O1 via the transition state TS3, forming a surface-adsorbed HgO species (IM3). This step is endothermic by 4.269 eV, with an activation barrier of 4.403 eV. In Pathway 2, the adsorbed Hg^0 atom similarly migrates to the adjacent O_2 site via TS4, yielding another HgO intermediate (IM4). This step is endothermic by 4.514 eV, with a corresponding energy barrier of 4.538 eV. The Hg-O bond lengths in IM3 and IM4 are 1.957 Å and 1.961 Å, respectively, suggesting the generation of HgO. In the final step (HgO (ads) \rightarrow

HgO), the formed HgO species desorbs from the LaMnO₃(010) surface, resulting in the generation of an oxygen vacancy (vac-LaMnO₃(010)). This desorption proceeds via two pathways: IM3 \rightarrow TS5 \rightarrow FS3 (Pathway 1) and IM4 \rightarrow TS6 \rightarrow FS4 (Pathway 2). Both steps are endothermic, with energy barriers of 1.670 eV and 1.539 eV, respectively. For the oxidation of Hg⁰ by lattice oxygen, the second step (Hg (ads) \rightarrow HgO (ads)) is identified as the rate-limiting step. The energy barrier for the rate-limiting step in Pathway 1 (4.403 eV) is slightly lower than that of Pathway 2 (4.538 eV), indicating that the surface lattice oxygen at the O₁ site exhibits higher oxidation activity toward Hg⁰.

In the case of Hg^0 oxidation by perpendicularly adsorbed O_2 (Fig. 9), the fundamental reaction steps are similar to those observed in Hg^0 oxidation by lattice oxygen. Based on the variations in adsorption sites for Hg^0 and HgO, a total of four different reaction pathways are identified. Under Pathways 1 and 2, the Hg^0 atom initially adsorbs onto a surface Mn site, forming intermediate IM5 with an exothermic adsorption energy of -0.274 eV. Subsequently, the Hg^0 atom reacts with the oxygen atom located above the adsorbed O_2 species, forming a surfacebound HgO species adsorbed on the Mn site (Pathway 1) or the subsurface oxygen atom (Pathway 2). The channels are IM5 \rightarrow TS7 \rightarrow IM6 (Pathway 1) and IM5 \rightarrow TS8 \rightarrow IM7 (Pathway 2), with corresponding energy barriers of 1.095 eV and 1.541 eV, respectively. Subsequently,

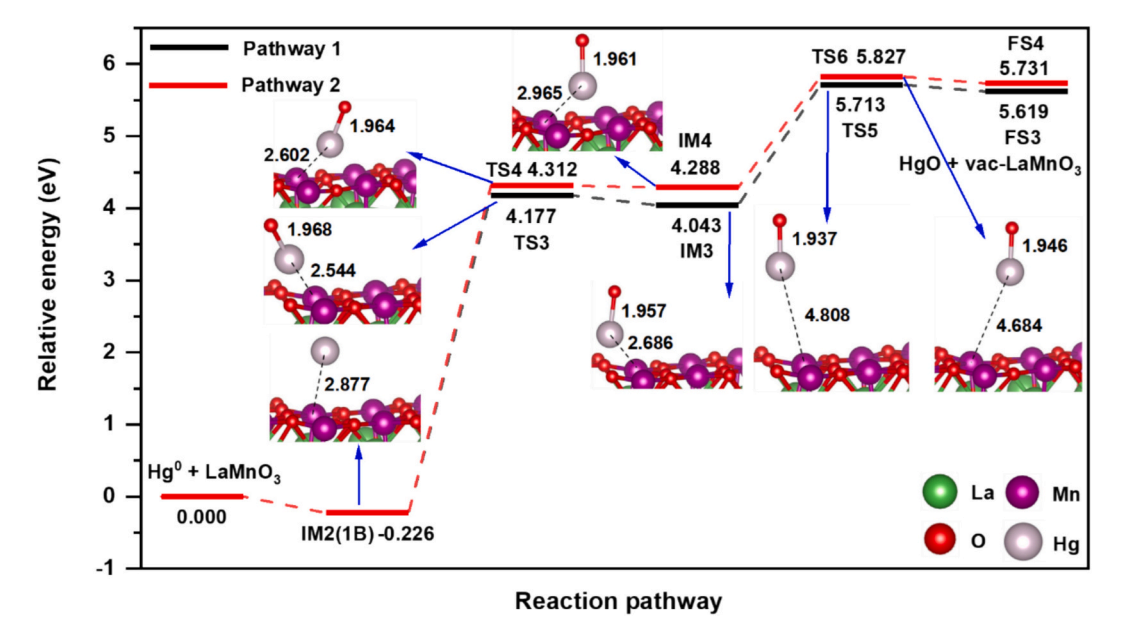


Fig. 8. Energy profiles and optimized structures of Hg^0 oxidation by lattice oxygen on $LaMnO_3(010)$ surface. The unit for bond length is Å.

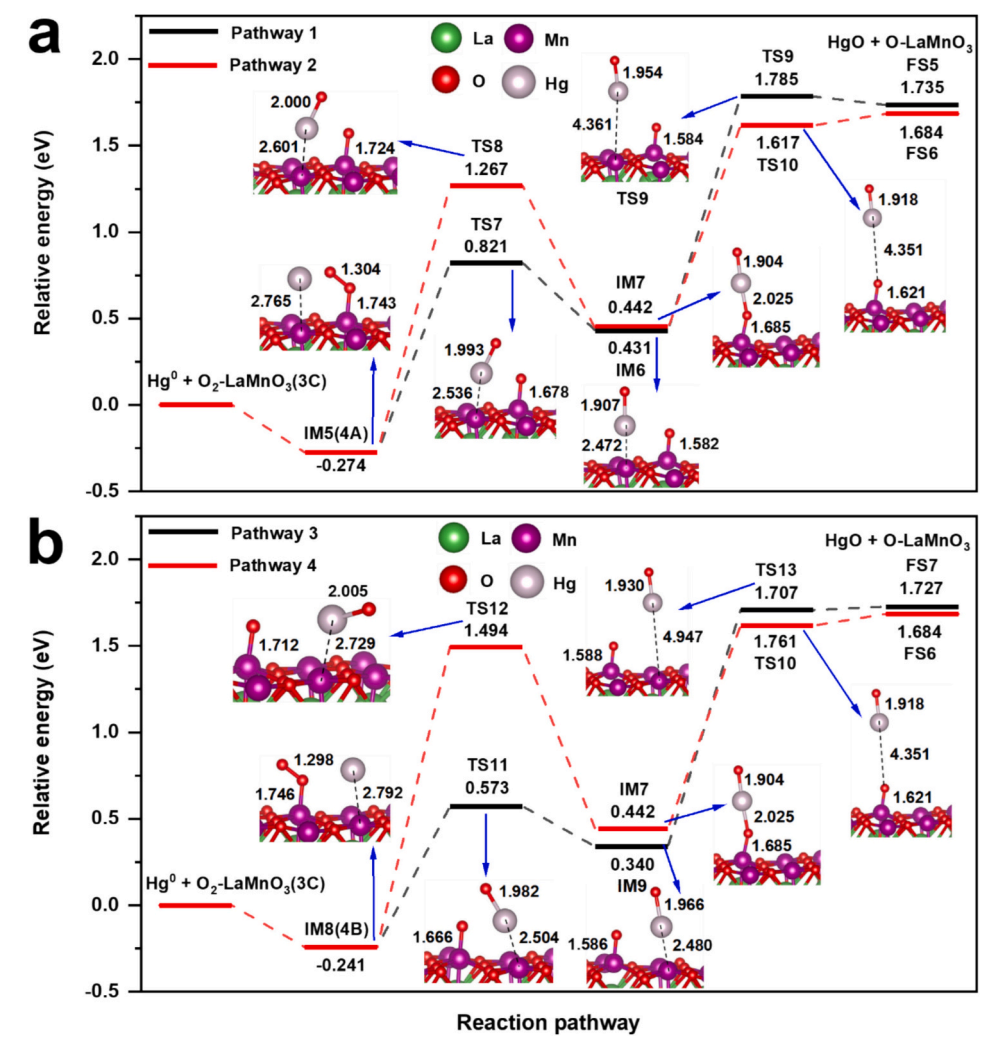


Fig. 9. Energy profiles and optimized structures of Hg⁰ oxidation by perpendicular adsorbed O₂ on LaMnO₃(010) surface. The unit for bond length is Å.

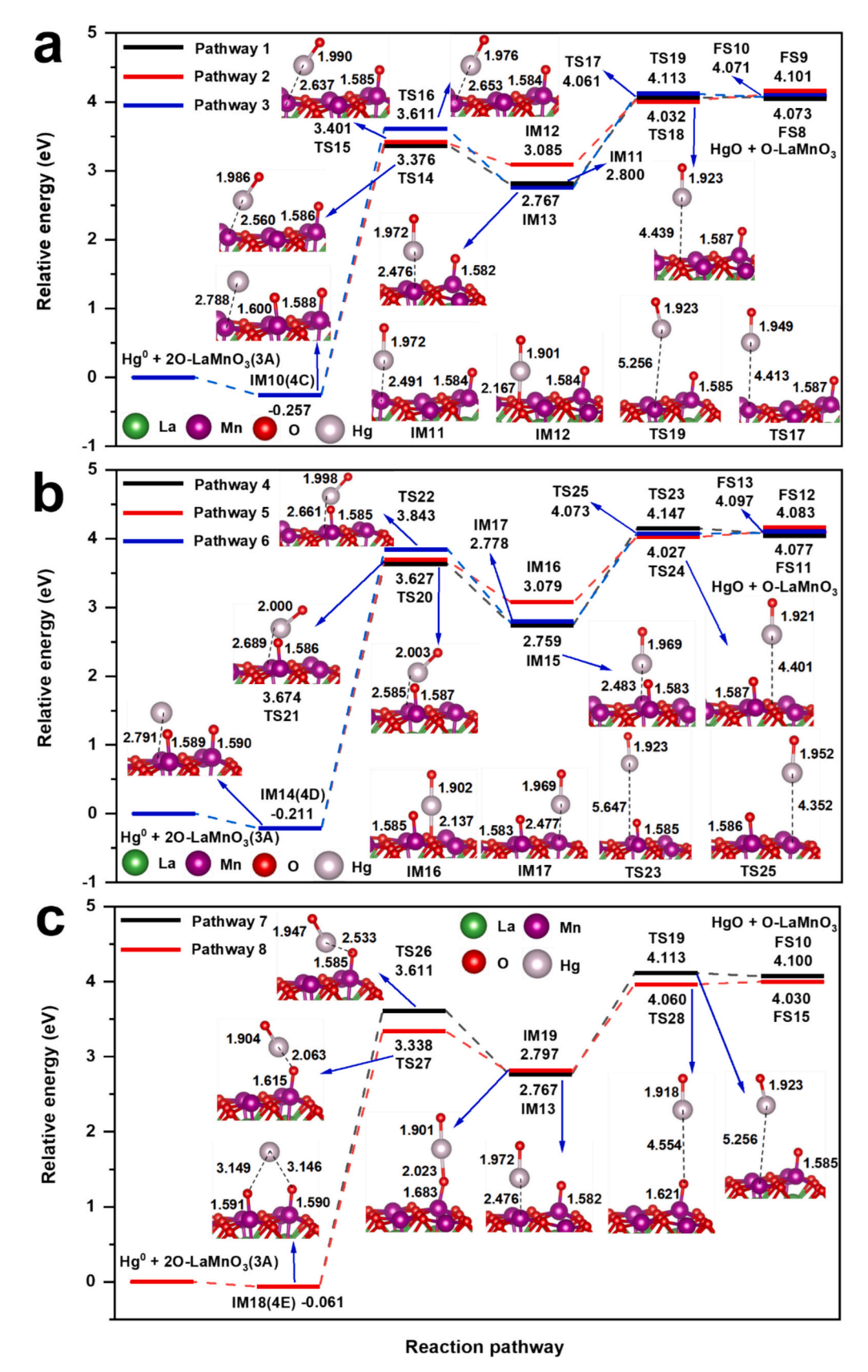


Fig. 10. Energy profiles and optimized structures of Hg⁰ oxidation by dissociative adsorbed O₂ on LaMnO₃(010) surface (3A). The unit for bond length is Å.

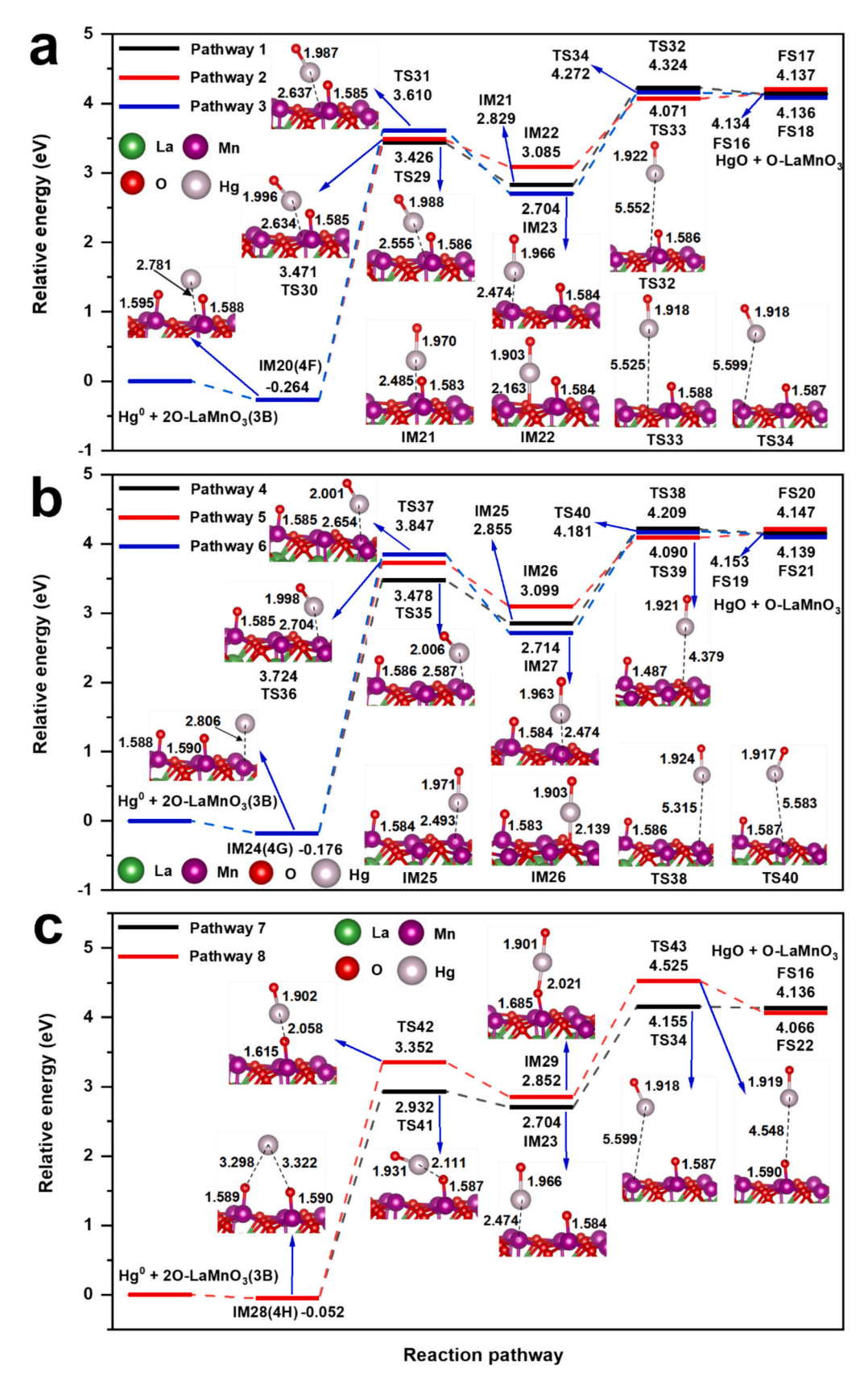


Fig. 11. Energy profiles and optimized structures of Hg⁰ oxidation by dissociative adsorbed O₂ on LaMnO₃(010) surface (3B). The unit for bond length is Å.

HgO desorbs from the surface through the reaction pathways IM6 → TS9 \rightarrow FS5 (Pathway 1) and IM7 \rightarrow TS10 \rightarrow FS6 (Pathway 2). The cleavage of the Hg-Mn and Hg-O bonds require overcoming energy barriers of 1.354 eV and 1.176 eV, respectively. The rate-limiting steps differ for the two pathways: IM6 \rightarrow TS9 \rightarrow FS5 in Pathway 1 and IM5 \rightarrow TS8 → IM7 in Pathway 2, with corresponding energy barriers of 1.354 eV and 1.541 eV, respectively. The reaction processes in Pathways 3 and 4 are generally similar to those in Pathways 1 and 2, with the primary difference being the Mn adsorption site for the Hg atom. In these pathways, Hg⁰ initially adsorbs onto a different surface Mn atom, forming intermediate IM8 with an adsorption energy of -0.209 eV. For Pathway 3, the reaction proceeds through IM8 \rightarrow TS11 \rightarrow IM9 \rightarrow TS13 \rightarrow FS7, while for Pathway 4, it follows IM8 \rightarrow TS12 \rightarrow IM7 \rightarrow TS10 \rightarrow FS6. The rate-limiting steps for these pathways are IM9 \rightarrow TS13 \rightarrow FS7 and IM8 \rightarrow $TS12 \rightarrow IM7$, with corresponding activation energy barriers of 1.367 eV and 1.735 eV, respectively. Based on the above analysis, Pathway 1 exhibits the lowest energy barrier for the rate-limiting step, indicating that it is the most favourable pathway for Hg^0 oxidation by perpendicularly adsorbed O2.

In the oxidation of Hg⁰ by dissociative adsorbed O₂ in Mn-O₁-Mn configuration (3A), eight possible reaction pathways were identified based on the different adsorption sites of Hg⁰ and generated HgO, as illustrated in Fig. 10. Among these, Pathways 1-3 start from the same initial adsorption configuration, IM10, in which the Hg atom is adsorbed with an energy of -0.257 eV. In Pathway 1, the surface O atom migrates toward the adsorbed Hg⁰ atom to form HgO. In Pathway 2, both the Hg⁰ atom and the O atom simultaneously migrate toward each other, forming HgO that subsequently adsorbs onto the oxygen site. In Pathway 3, the Hg⁰ atom moves toward the O atom to form HgO. Finally, the forming HgO species desorbs from the surface. The corresponding reaction routes are IM10 \rightarrow TS14 \rightarrow IM11 \rightarrow TS17 \rightarrow FS8 for Pathway 1, $IM10 \rightarrow TS15 \rightarrow IM12 \rightarrow TS18 \rightarrow FS9$ for Pathway 2, and $IM10 \rightarrow TS16$ \rightarrow IM13 \rightarrow TS19 \rightarrow FS10 for Pathway 3. In all three cases, the second step (Hg (ads) → HgO (ads)) is the rate-limiting step, with energy barriers of 3.633 eV, 3.657 eV and 3.868 eV, respectively. The reaction processes in Pathways 4–6 are similar to those in Pathways 1–3, with the primary difference being the initial Mn adsorption site of the Hg⁰ atom. In all three cases, the conversion from Hg (ads) to HgO (ads) remains the rate-limiting step, with energy barriers of 3.838 eV, 3.885 eV and 4.053 eV, respectively. In Pathways 7 and 8, the Hg atom is initially adsorbed above and between two dissociated oxygen atoms, forming the IM18 configuration with an exothermic energy of 0.061 eV. In Pathway 7, the Hg atom migrates toward one adsorbed O atom to form HgO, which binds to the Mn atom with the Hg-Mn bond length of 2.476 Å. In Pathway 8, one of the O atoms migrates to the Hg atom forming HgO, which is adsorbed on the other surface O atom, with the O-Hg bond length of 2.023 Å. After that, the formed HgO desorbs from the surface. The intermediate transitions for Pathways 7 and 8 proceed as follows: IM18 \rightarrow TS26 \rightarrow IM13 \rightarrow TS19 \rightarrow FS10 and IM18 \rightarrow TS27 \rightarrow IM19 \rightarrow TS28 \rightarrow FS15, respectively. In both cases, the second step Hg (ads) \rightarrow HgO (ads) is the rate-limiting step, with energy barriers of 3.672 eV and 3.399 eV, respectively. Besides, the second step (Hg (ads) \rightarrow HgO (ads)) serves as the rate-limiting step across all eight pathways. Among them, Pathway 8 exhibits the lowest energy barrier for the rate-determining step, 3.399 eV, indicating it is the most thermodynamically favourable pathway.

The oxidation of Hg^0 by dissociative adsorbed O_2 in the Mn-O₂-Mn configuration (3B) proceeds similarly to that in the Mn-O₁-Mn configuration (3A), with the primary difference arising from the relative positions of the two adsorbed oxygen atoms. A total of eight reaction pathways are identified. In all cases, the step involving the conversion from Hg (ads) to HgO (ads) is the rate-limiting step. Among these, Pathway 7 exhibits the lowest activation barrier of 2.984 eV, indicating it is the most favourable reaction route.

In summary, the oxidation of Hg⁰ by four distinct types of oxygen species on the LaMnO₃(010) surface is found to be endothermic in all

cases, with overall reaction energies ($E_{\rm all}$) exceeding zero. The impact of individual reaction pathways on the total reaction enthalpy is relatively minor within each oxidation type. Among them, oxidation via perpendicularly adsorbed O_2 exhibits markedly lower activation barriers and reaction energies, consistent with previous studies [27]. Notably, Pathway 1 in this category shows the lowest rate-limiting barrier (1.354 eV), making it the most favourable route for Hg^0 oxidation. Furthermore, HCl significantly influences Hg^0 oxidation. A comparison with HCl oxidation results reveal that the energy barrier for Hg^0 oxidation by HCl on the LaMnO₃(010) surface is 0.74 eV [26], substantially lower than that for O_2 (1.354 eV). This suggests that Hg—Cl interactions are thermodynamically more favourable than Hg—O interactions, which agrees well with previous studies [27,43].

4. Conclusions

In this study, DFT calculations were employed to investigate the oxidation mechanisms of elemental mercury (Hg⁰) on the LaMnO₃(010) surface by four types of oxygen species: lattice oxygen, perpendicularly adsorbed O2, dissociative adsorbed O2 in the Mn-O1-Mn configuration, and dissociative adsorbed O_2 in the Mn-O₂-Mn configuration. We first examined the adsorption behaviour of Hg⁰, HgO and O₂ on LaMnO₃(010), suggesting that all of them can be chemisorbed on the surface. Additionally, the dissociation mechanisms of O₂ were explored. Subsequently, the adsorption configurations of Hg⁰ on O₂-covered $LaMnO_3(010)$ surfaces were analysed. A total of 22 possible reaction pathways were systematically investigated for Hg⁰ oxidation by the four types of oxygen species. Among them, oxidation by perpendicularly adsorbed O2 is found to be kinetically more favourable. Notably, Pathway 1 within this category exhibits the lowest rate-limiting energy barrier (1.354 eV), making it the most favourable route for Hg⁰ oxidation. It is worth noting that the PBE functional, while being widely used for transition metal oxides, has known limitations in accurately describing strongly correlated electron systems such as underestimating band gaps and overly delocalizing localized d-electrons. In future work, more advanced methods such as DFT + U or hybrid functionals may be employed to improve the description of localized d-electrons and enhance the quantitative accuracy of the calculations. Furthermore, real flue gas typically contains additional components such as H₂O, Cl₂ and SO₂, which may influence the oxidation behaviour of Hg⁰. Therefore, further studies are necessary to elucidate the effects of these species on Hg⁰ oxidation over LaMnO₃ surface.

CRediT authorship contribution statement

Zhongze Bai: Writing – original draft, Visualization, Validation, Software, Methodology, Investigation, Formal analysis, Data curation, Conceptualization. **Kai H. Luo:** Writing – review & editing, Supervision, Resources, Project administration, Funding acquisition.

Declaration of competing interest

The authors declare that they have no known competing financial interests or personal relationships that could have appeared to influence the work reported in this paper.

Acknowledgements

The research is supported by Carbon Neutrality and Energy System Transformation (CNEST) Programme led by Tsinghua University. Support from the UK Engineering and Physical Sciences Research Council under the project "UK Consortium on Mesoscale Engineering Sciences (UKCOMES)" (Grant No. EP/X035875/1) is also acknowledged. This work made use of computational support by CoSeC, the Computational Science Centre for Research Communities, through UKCOMES.

Data availability

Data will be made available on request.

References

- [1] O. Hoegh-Guldberg, D. Jacob, M. Taylor, T. Guillén Bolaños, M. Bindi, S. Brown, et al., The human imperative of stabilizing global climate change at 1.5 C, Science 365 (6459) (2019) eaaw6974.
- [2] N. Shehzad, M. Tahir, K. Johari, T. Murugesan, M. Hussain, A critical review on TiO2 based photocatalytic CO2 reduction system: strategies to improve efficiency, J CO₂ Util 26 (2018) 98–122.
- [3] W. Gao, S. Liang, R. Wang, Q. Jiang, Y. Zhang, Q. Zheng, et al., Industrial carbon dioxide capture and utilization: state of the art and future challenges, Chem. Soc. Rev. 49 (23) (2020) 8584–8686.
- [4] J. Adanez, A. Abad, F. Garcia-Labiano, P. Gayan, L.F. De Diego, Progress in chemical-looping combustion and reforming technologies, Prog. Energy Combust. Sci. 38 (2) (2012) 215–282.
- [5] B. Tang, H. Xu, K.-K. Wong, K.-F. Tong, Y. Zhang, C.-B. Chae, Fluid antenna enabling secret communications, IEEE Commun. Lett. 27 (6) (2023) 1491–1495.
- [6] Y. Li, J. Liu, F. Liu, Y. Yang, R. Fang, Mechanistic study of the effect of oxygen vacancy and sulfur poisoning on the reaction of copper ferrite spinel with CO during chemical-looping combustion, Fuel 299 (2021) 120931.
- [7] J. Adánez, A. Abad, T. Mendiara, P. Gayán, L. De Diego, F. García-Labiano, Chemical looping combustion of solid fuels, Prog. Energy Combust. Sci. 65 (2018) 6–66.
- [8] A. Cabello, A. Abad, M.T. Izquierdo, P. Gayán, L.F. de Diego, F. García-Labiano, et al., Qualification of operating conditions to extend oxygen carrier utilization in the scaling up of chemical looping processes, Chem. Eng. J. 430 (2022) 132602.
- [9] S. Daneshmand-Jahromi, M.H. Sedghkerdar, N. Mahinpey, A review of chemical looping combustion technology: fundamentals, and development of natural, industrial waste, and synthetic oxygen carriers, Fuel 341 (2023) 127626.
- [10] J. Yan, S. Wang, B. Hu, H. Zhang, L. Qiu, W. Liu, et al., Review of chemical looping technology for energy conservation and utilization: CO2 capture and energy cascade utilization, J. Environ. Chem. Eng. (2024) 112602.
- [11] S.A. Hosseini, B. Mehri, A. Niaei, B. Izadkhah, C. Alvarez-Galvan, J.G.L. Fierro, Selective catalytic reduction of NO x by CO over LaMnO 3 nano perovskites prepared by microwave and ultrasound assisted sol–gel method, J. Sol-Gel Sci. Technol. 85 (2018) 647–656.
- [12] C. Sun, J.A. Alonso, J. Bian, Recent advances in perovskite-type oxides for energy conversion and storage applications, Adv. Energy Mater. 11 (2) (2021) 2000459.
- [13] X. Zhu, K. Li, L. Neal, F. Li, Perovskites as geo-inspired oxygen storage materials for chemical looping and three-way catalysis: a perspective, ACS Catal. 8 (9) (2018) 8213–8236.
- [14] Q. Ji, L. Bi, J. Zhang, H. Cao, X.S. Zhao, The role of oxygen vacancies of ABO 3 perovskite oxides in the oxygen reduction reaction, Energ. Environ. Sci. 13 (5) (2020) 1408–1428
- [15] X. Ma, J. Liu, Y. Yang, Experimental and theoretical studies on the reactivity and reaction mechanism of LaMnO3 with CO in chemical looping combustion, J. Energy Inst. 112 (2024) 101462.
- [16] X. Yan, J. Liu, Y. Yang, Z. Wang, Y. Zheng, A catalytic reaction scheme for NO reduction by CO over Mn-terminated LaMnO3 perovskite: a DFT study, Fuel Process. Technol. 216 (2021) 106798.
- [17] Z. Sarshar, F. Kleitz, S. Kaliaguine, Novel oxygen carriers for chemical looping combustion: La 1 – x Ce x BO 3 (B= Co, Mn) perovskites synthesized by reactive grinding and nanocasting, Energ. Environ. Sci. 4 (10) (2011) 4258–4269.
- [18] Z. Sarshar, Z. Sun, D. Zhao, S. Kaliaguine, Development of sinter-resistant core-shell LaMn x Fe1-x O3@ mSiO2 oxygen carriers for chemical looping combustion, Energy Fuel 26 (5) (2012) 3091–3102.
- [19] E.F. Iliopoulou, C. Matsouka, E. Pachatouridou, F. Papadopoulou, A. Psarras, A. Evdou, et al., Novel La1 – x ca x MnO3 perovskite materials for chemical looping combustion applications, Int. J. Energy Res. 46 (14) (2022) 20386–20400.
- [20] X. Ma, J. Liu, Y. Yang, X. Wang, Review and outlook of theoretical understanding on pollutants reaction mechanism during chemical looping combustion, Energy Fuel 38 (16) (2024) 15055–15068.

- [21] Z. Liu, J. Zhou, L. Zhou, B. Li, T. Wang, H. Liu, A review on mercury removal in chemical looping combustion of coal, Sep. Purif. Technol. 337 (2024) 126352.
- [22] WHO, WHO. https://www.who.int/news-room/fact-sheets/detail/mercury-and-health.
- [23] UNEP, UNEP. https://www.unep.org/globalmercurypartnership/what-we-do/mercury-releases-coal-combustion.
- [24] F. Shen, J. Liu, Z. Zhang, J. Dai, On-line analysis and kinetic behavior of arsenic release during coal combustion and pyrolysis, Environ. Sci. Technol. 49 (22) (2015) 13716–13723.
- [25] Y. Yang, J. Liu, F. Shen, L. Zhao, Z. Wang, Y. Long, Kinetic study of heterogeneous mercury oxidation by HCl on fly ash surface in coal-fired flue gas, Combust. Flame 168 (2016) 1–9.
- [26] Z. Wang, J. Liu, Y. Yang, Y. Yu, X. Yan, Z. Zhang, Insights into the catalytic behavior of LaMnO3 perovskite for Hg0 oxidation by HCl, J. Hazard. Mater. 383 (2020) 121156.
- [27] Z. Wang, J. Liu, Y. Yang, F. Liu, J. Ding, Heterogeneous reaction mechanism of elemental mercury oxidation by oxygen species over MnO2 catalyst, Proc. Combust. Inst. 37 (3) (2019) 2967–2975.
- [28] G. Kresse, J. Furthmüller, Efficiency of ab-initio total energy calculations for metals and semiconductors using a plane-wave basis set, Comput. Mater. Sci. 6 (1) (1996) 15-50
- [29] G. Kresse, J. Hafner, Ab initio molecular dynamics for liquid metals, Phys. Rev. B 47 (1) (1993) 558.
- [30] J.P. Perdew, K. Burke, M. Ernzerhof, Generalized gradient approximation made simple, Phys. Rev. Lett. 77 (18) (1996) 3865.
- [31] G. Henkelman, B.P. Uberuaga, H. Jónsson, A climbing image nudged elastic band method for finding saddle points and minimum energy paths, J. Chem. Phys. 113 (22) (2000) 9901–9904.
- [32] V. Wang, N. Xu, J.-C. Liu, G. Tang, W.-T. Geng, VASPKIT: a user-friendly interface facilitating high-throughput computing and analysis using VASP code, Comput. Phys. Commun. 267 (2021) 108033.
- [33] W. Yi, G. Tang, X. Chen, B. Yang, X. Liu, Qvasp: a flexible toolkit for VASP users in materials simulations, Comput. Phys. Commun. 257 (2020) 107535.
- [34] K. Momma, F. Izumi, VESTA: a three-dimensional visualization system for electronic and structural analysis, Applied Crystallography. 41 (3) (2008) 653–658.
- [35] A. Jain, S.P. Ong, G. Hautier, W. Chen, W.D. Richards, S. Dacek, et al., Commentary: the materials project: a materials genome approach to accelerating materials innovation, APL Mater. 1 (1) (2013).
- [36] A.L. Gavin, G.W. Watson, Modelling oxygen defects in orthorhombic LaMnO 3 and its low index surfaces, Phys. Chem. Chem. Phys. 19 (36) (2017) 24636–24646.
- [37] S. Piskunov, E. Heifets, T. Jacob, E.A. Kotomin, D.E. Ellis, E. Spohr, Electronic structure and thermodynamic stability of LaMnO 3 and La 1 x Sr x MnO 3 (001) surfaces: ab initio calculations, Phys. Rev. B: Condens. Matter Mater. Phys. 78 (12) (2008) 121406.
- [38] H. Xu, Z. Qu, C. Zong, F. Quan, J. Mei, N. Yan, Catalytic oxidation and adsorption of Hg0 over low-temperature NH3-SCR LaMnO3 perovskite oxide from flue gas, Appl. Catal. Environ. 186 (2016) 30–40.
- [39] Z. Zhou, X. Liu, B. Zhao, H. Shao, Y. Xu, M. Xu, Elemental mercury oxidation over manganese-based perovskite-type catalyst at low temperature, Chem. Eng. J. 288 (2016) 701–710.
- [40] J. Yang, M. Zhang, H. Li, W. Qu, Y. Zhao, J. Zhang, Simultaneous NO reduction and Hg0 oxidation over La0. 8Ce0. 2MnO3 perovskite catalysts at low temperature, Ind. Eng. Chem. Res. 57 (29) (2018) 9374–9385.
- [41] X. Deng, B.K. Min, A. Guloy, C.M. Friend, Enhancement of O2 dissociation on au (111) by adsorbed oxygen: implications for oxidation catalysis, J. Am. Chem. Soc. 127 (25) (2005) 9267–9270.
- [42] S. Qiao, J. Chen, J. Li, Z. Qu, P. Liu, N. Yan, et al., Adsorption and catalytic oxidation of gaseous elemental mercury in flue gas over MnO x/alumina, Industrial & engineering chemistry research. 48 (7) (2009) 3317–3322.
- [43] D. Jampaiah, S.J. Ippolito, Y.M. Sabri, J. Tardio, P. Selvakannan, A. Nafady, et al., Ceria-zirconia modified MnO x catalysts for gaseous elemental mercury oxidation and adsorption, Cat. Sci. Technol. 6 (6) (2016) 1792–1803.